frontiers | Frontiers in Bioengineering and Biotechnology

TYPE Original Research
PUBLISHED 09 January 2023
DOI 10.3389/fbioe.2022.1016001

OPEN ACCESS

EDITED BY
Junchao Wei,
Nanchang University, China

REVIEWED BY
Meng Tian,
Sichuan University, China
Yuangang Liu,
Huaqiao University, China

*CORRESPONDENCE
Hao Wang,
wanghaosci@163.com

†These authors have contributed equally to this work

SPECIALTY SECTION
This article was submitted to Biomaterials, a section of the journal Frontiers in Bioengineering and Biotechnology

RECEIVED 10 August 2022
ACCEPTED 22 November 2022
PUBLISHED 09 January 2023

CITATION
Bai X, Yu J, Xiao J, Wang Y, Li Z and Wang H (2023), Antibacterial intraosseous implant surface coating that responds to changes in the bacterial microenvironment. *Front. Bioeng. Biotechnol.* 10:1016001. doi: 10.3389/fbioe.2022.1016001

Antibacterial intraosseous implant surface coating that responds to changes in the bacterial microenvironment

Xin Bai[1†], Jiawei Yu[2†], Jie Xiao[1], Yanping Wang[1], Zhe Li[1] and Hao Wang[3*]

[1]Jiande First People's Hospital, Hangzhou, Zhejiang, China, [2]Zhuji Affiliated Hospital of Wenzhou Medical University, Shaoxing, Zhejiang, China, [3]Department of Orthopedics, Quanzhou First Hospital Affiliated of Fujian Medical University, Quanzhou, Fujian, China

Bone implant-associated infection is one of the most challenging problems encountered by orthopedic surgeons. There is considerable interest in the development of drug-loaded antibacterial coatings for the surfaces of metal implants. However, it is difficult to achieve the stable local release of an effective drug dose for many antibacterial coatings. In the present study, analyses of the thickness and water contact angle of multiple layers confirmed the successful assembly of multilamellar membrane structures. Measurement of the zone of bacterial inhibition indicated gradual degradation of the (montmorillonite [MMT]/hyaluronic acid [HA])$_{10}$ multilamellar film structure with concentration-dependent degradation during incubation with hyaluronidase solution and *Staphylococcus aureus*. *In vivo* results resembled the *in vitro* results. Overall, the findings confirm that the (MMT/HA-rifampicin)$_{10}$ multilamellar film structure exhibits good antibacterial properties and excellent biocompatibility. Further studies of the clinical potential of the antibacterial coating prepared in this experiment are warranted.

KEYWORDS

infection, antibacterial coating, *Staphylococcus aureus*, layer-by-layer, microenvironment

1 Introduction

Since the introduction of various metallic and non-metallic fixation materials in the field of orthopedics, and particularly with the development of internal and external fixation over the past century, advances in materials science and medical techniques have led to the increasing use of orthopedic surgery (Berger et al., 2016; Li et al., 2017). However, bone and soft tissue infections remain among the most challenging complications of orthopedic surgery (Neumann et al., 2016; Pickett et al., 2018). In cases of open fractures, various fixation devices (e.g., plate screws, external fixation brackets, and intramedullary nails) may contribute to infection (Amerstorfer et al., 2017; Perez-Jorge et al., 2017). Closed fractures have infection rates of approximately 1.5%, whereas open fractures have infection rates of 3–40% (Neumann et al., 2016; Kendall and

Gorgone, 2018). The incidence of trauma-related open fractures is increasing (Tessier et al., 2016). Approximately 60% of open fractures are contaminated by bacteria at the time of injury (Caroom et al., 2018). Fixation-related infections can also cause serious adverse consequences for patients, potentially requiring systemic antibiotics, multiple debridement-and-revision surgeries, extended hospital stays, and/or amputations; they may also result in death (Barnett et al., 2016; Klein et al., 2016). Therefore, fixation-related infections have become a major research focus in the fields of orthopedics, microbiology, biomaterials, and drug development (Jones et al., 2016; Sugii et al., 2017).

The local preventive or therapeutic application of antibiotics has received considerable attention for the treatment of internal fixation-related infections (Flamant et al., 2016). Intravenous infusion of antibiotics based on the results of drug sensitivity testing is a common clinical treatment method, but systemic drug administration can only achieve low concentrations in lesions while potentially damaging areas such as the liver, kidney, and ears (Girmenia and Iori, 2017; Kyriakidis et al., 2017). Therefore, the application of drug-loaded antibacterial coatings on the surfaces of metal implants has been proposed to aid in preventing infection and avoiding side effects associated with systemic administration (Li et al., 2016). Jennings et al. (2015) mixed vancomycin and amikacin into lecithin to form a uniform solution that could coat the surface of titanium metal. They found that the drugs could be stably released for approximately six days, and their system exhibited *in vitro* antibacterial activity against *Staphylococcus aureus*. Braem et al. (2015) used titanium with a pore structure as a drug carrier, then integrated it into a mesoporous SiO_2 diffusion barrier to control drug release on the titanium metal surface. Although this method resolved the problem of drug burst release, the drug release time remained short. Hirschfeld et al. (2017) used plasma vapor deposition to deposit vertically aligned carbon nanotubes approximately 700 nm long and 10–200 nm in diameter on the surface of titanium; the tubes were used to carry rifampicin (RFP). Their experiments confirmed the antibacterial ability of the RFP from these carbon nanotubes against *Staphylococcus epidermidis*. The greatest limitation of using these surface coatings as antibacterial drug carriers is that they generally do not allow the stable local release of effective drug doses. There is often a burst release in the early stages of drug release, and it is difficult to maintain accurate drug release for an extended duration. There has been considerable progress in the construction of stimulus-sensitive drug delivery systems on the surfaces of biological materials (Huang et al., 2016; Wang et al., 2016), and numerous drug delivery systems based on enzymes, temperature, and pH sensitivity have been constructed (Sun et al., 2021). These stimulus-sensitive drug delivery systems can control drug release and avoid drug resistance caused by excessive short-term release or minimal long-term release. The microenvironment of bacterial infection has multiple unique biological characteristics, including the abnormal expression of some enzymes and the specific release of toxins (Wang et al., 2018a). These specific biological characteristics can be used to prepare smart drug delivery systems with appropriate microenvironmental responses to ensure controlled release and accumulation of antibacterial drugs at the site of infection (Aycan and Alemdar, 2018). Layer-by-layer self-assembly based on multisubstance interactions is a useful method for the formation of nanostructured multilamellar films (Chen et al., 2017). External stimuli can achieve the selective embedding of substances and the intelligent controlled release of drugs from multilamellar films (Mable et al., 2018).

S. aureus is the main species of pathogenic bacteria encountered after surgery or trauma and the primary species involved in endosseous implant-related bone, joint, and soft tissue infections (Gundtoft et al., 2017; Araújo et al., 2018). The entry of *S. aureus* into lymphatic vessels or blood can cause sepsis. RFP, which has high antibacterial activity against various Gram-positive bacteria (Branch-Elliman et al., 2017), is a key antibiotic for treating severe *S. aureus* infections. It has an important role in clinical therapy and is an ideal antibiotic for topical application (Downes et al., 2017). During bacterial infection, the surrounding environment secretes large amounts of hyaluronidase (HAS) and phospholipase (Seroussi et al., 2018; Liu et al., 2021). Montmorillonite (MMT)/hyaluronic acid (HA) multilamellar film actively disintegrates in the presence of infection (Wang et al., 2018b). MMT is a typical clay mineral with a unique crystal structure that provides it with a high cation exchange capacity and a high expansion capacity; thus, it is widely used in various fields (Enteshari Najafabadi and Bagheri, 2017). Because of its high specific surface area, MMT can additionally be included in multilamellar films to load drugs at high concentrations and prevent rapid release (Qiao et al., 2016; Chabbi et al., 2018). HA is an acidic mucopolysaccharide that is widely distributed in the human body. It solubilizes readily in water, where it forms an acidic solution with a considerable negative charge. HA has good biocompatibility and various clinical uses (e.g., as a lubricant in joint surgery and a moisturizing agent in eye surgery) (Friedrich and Washburn, 2017; Hwang et al., 2017). In the present study, drug-loaded polyelectrolyte multilayers of $(MMT/HA\text{-}RFP)_{10}$ were fabricated in a layer-by-layer manner and exhibited HAS release-induced degradation in the presence of infection.

2 Materials and methods

2.1 Reagents and materials

MMT was obtained from Zhejiang Sanding Technology Co., Ltd. (Zhejiang, China). HA was purchased from Freda Biochem Co., Ltd. (Shandong, China). RFP and polyethyleneimine (Mw: 25 kDa) were purchased from Sigma-Aldrich (St. Louis, MO,

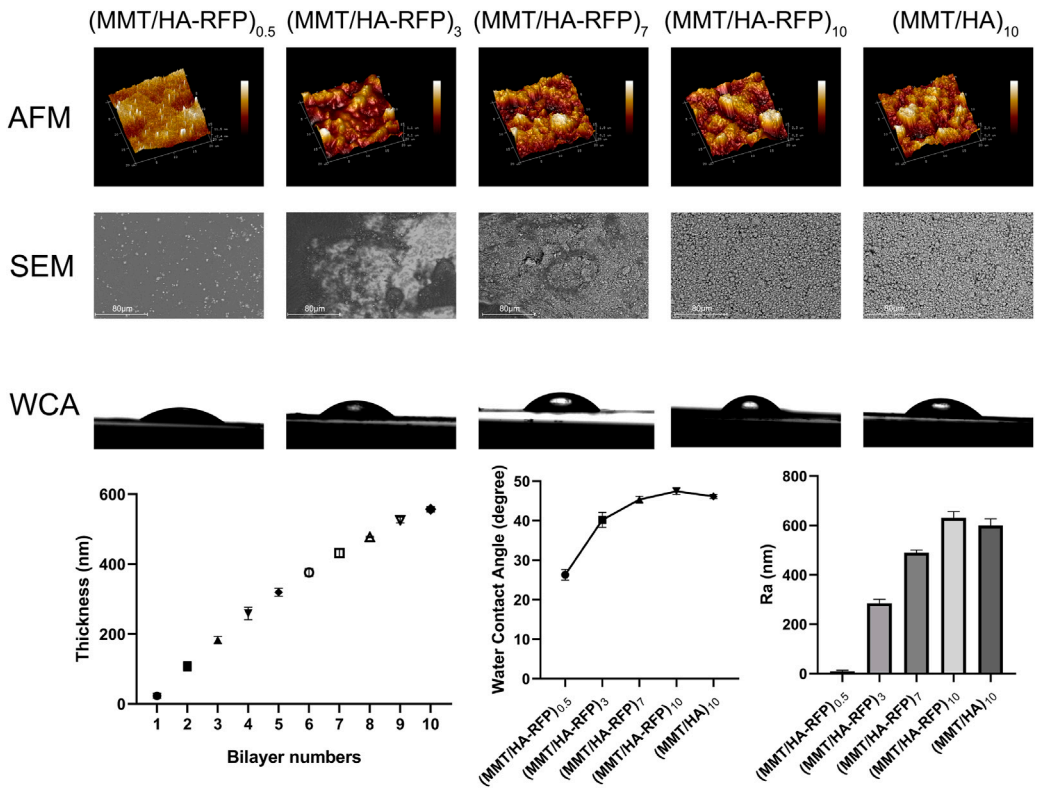

FIGURE 1
Atomic force microscopy (AFM), SEM, water contact angle (WCA), and thickness analysis of multilamellar membrane structures during co-assembly.

United States). Titanium Kirschner wires (K-wires; 1.25 mm) were purchased from MK Medical GmbH & Co. (Emmingen-Liptingen, Baden-Württemberg, Germany). Luria-Bertani agar and Luria-Bertani broth were purchased from Difco Laboratories (Detroit, MI, United States).

2.2 Construction of polyelectrolyte multilayers

The substrates were ultrasonically cleaned in acetone and in ethanol for 2 h each, then dried with compressed air. MMT stock solution (0.5 mg/ml, pH = 2.5) was prepared. Next, HA and RFP were separately dissolved at a concentration of 1.0 mg/ml in deionized water. Before assembly, the reaction solutions were dispersed by ultrasonication for 2 h. All substrates were subsequently deposited in polyethyleneimine solution (3 mg/ml, 20 min) as a precursor, then immersed alternately in MMT solution and HA-RFP solution for 15 min each at room temperature. Finally, the obtained hybrid multilamellar films were dried under a stream of nitrogen gas. This immersion cycle corresponded to the deposition of one bilayer. The above steps were repeated 10 times to yield $(MMT/HA\text{-}RFP)_{10}$ multilamellar membrane structures.

2.3 Characterization of materials

We tested the following polymer coatings: $(MMT/HA\text{-}RFP)_{0.5}$, $(MMT/HA\text{-}RFP)_3$, $(MMT/HA\text{-}RFP)_7$, $(MMT/HA\text{-}RFP)_{10}$, and $(MMT/HA)_{10}$. The surface roughness of silicon wafers, the substrate material, was measured by atomic force microscopy. Additionally, scanning electron microscopy (SEM) was performed to examine the surface morphology of each sample. To determine the wetting properties of the multilamellar film surfaces, water contact angles were measured using a video optical contact angle measuring

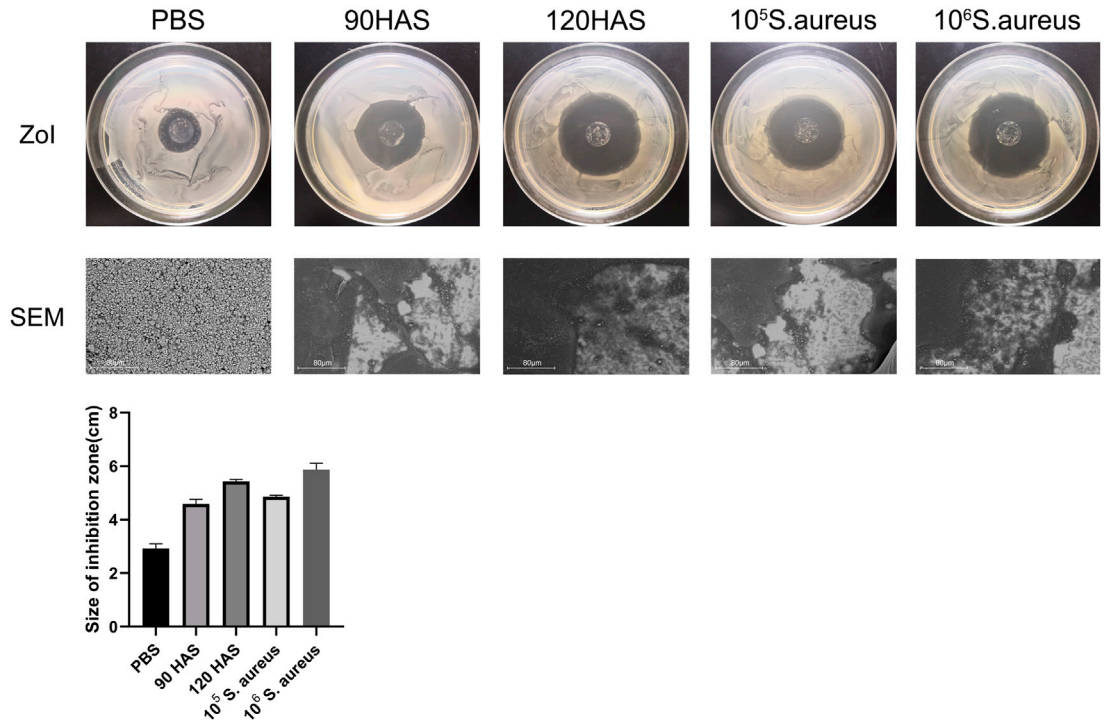

FIGURE 2
ZOI and SEM of $(MMT/HA\text{-}RFP)_{10}$ multilamellar film-coated glass slides after immersion in 0.01 M PBS, HAS, and *Staphylococcus aureus* solutions.

device (OCA15pro; DataPhysics Co., Filderstadt, Germany) in air at room temperature (25°C). The mean value of each multilamellar film structure was calculated from the measurements at three different locations. To confirm the successful assembly of multilamellar membrane structures, the thickness of $(MMT/HA\text{-}RFP)_n$ deposited in each layer was measured by spectroscopic ellipsometry (M-2000 DITM; J.A. Woollam, Lincoln, NE, United States).

2.4 Zone of inhibition measurement and SEM

Glass slides were selected as the substrate material in this study. Layer-by-layer self-assembled multilamellar films were prepared using the method described above. The multilamellar films were immersed for two days in 0.01 M phosphate-buffered saline (PBS), HAS solution, and *S. aureus* solution. At the end of the soaking period, all samples were removed and dried in an oven. *S. aureus* was grown from broth on nutrient agar, then plated on Luria-Bertani agar. Growth inhibition was verified based on the zone of inhibition (ZOI) after incubation at 37°C for 24 h. SEM was used to examine changes in the $(MMT/HA\text{-}RFP)_{10}$ multilamellar coating on the surface of the glass slides.

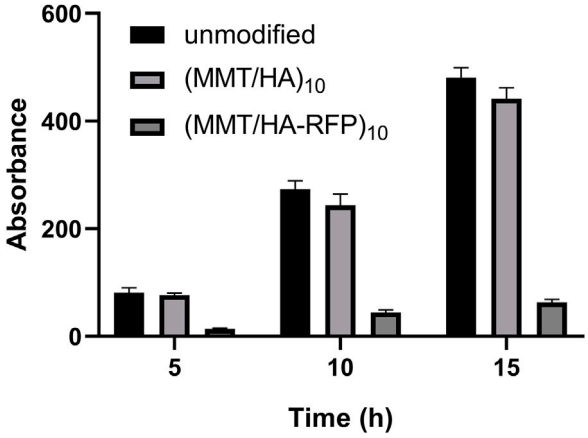

FIGURE 3
Determination of biofilm formation after immersion with unmodified, $(MMT/HA)_{10}$-coated, and $(MMT/HA\text{-}RFP)_{10}$ multilamellar film-coated silicon wafers at various time points.

2.5 Assessment of biofilm formation

Unmodified silicon wafers, as well as $(MMT/HA)_{10}$ and $(MMT/HA\text{-}RFP)_{10}$ multilamellar film silicon wafers, were

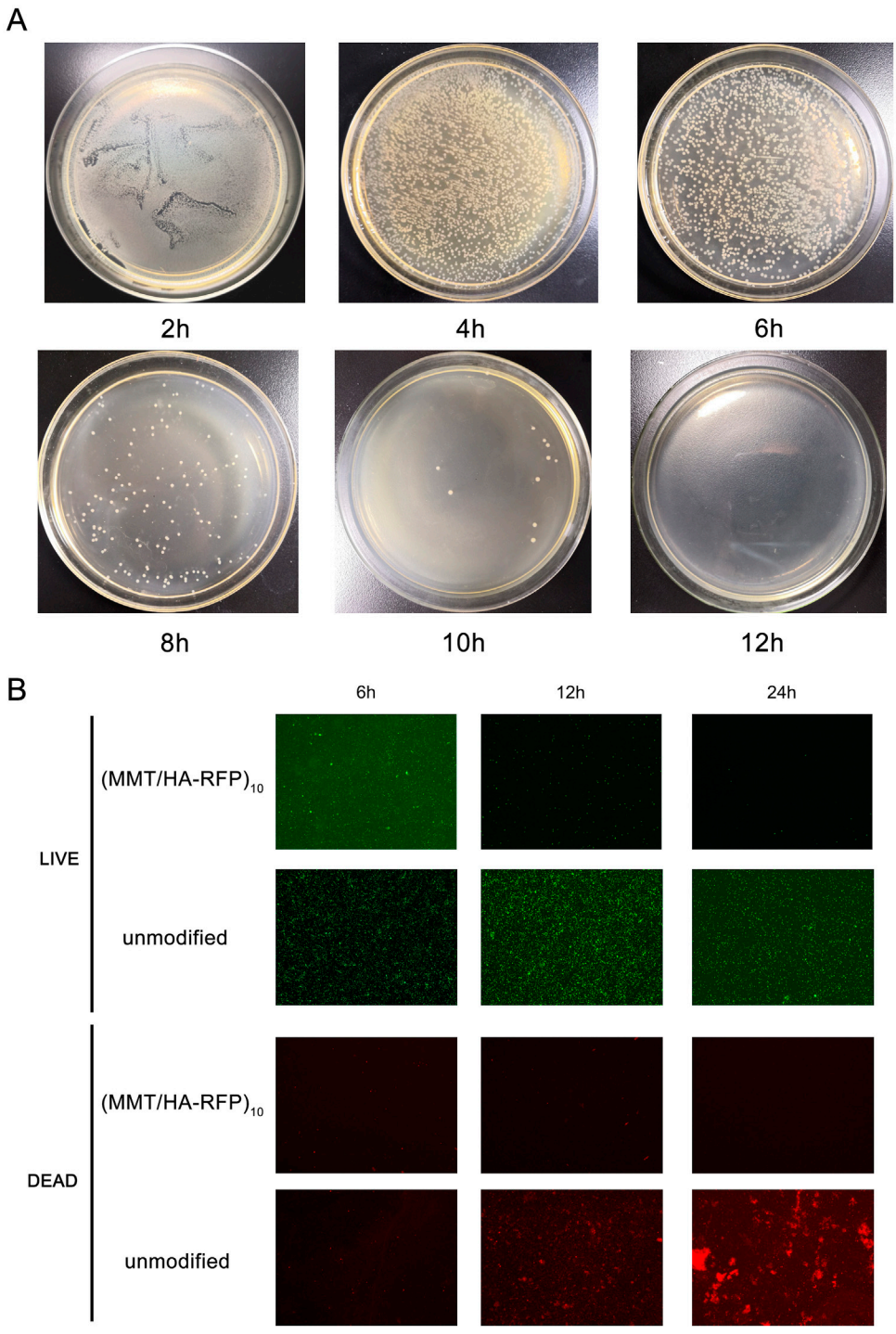

FIGURE 4
(A) Shaking flask culture and **(B)** live/dead staining assay.

prepared as three parallel samples, then immersed in 2 ml of *S. aureus* suspension [10 colony-forming units/ml (Kendall and Gorgone, 2018)] and incubated at 37°C for 5, 10, or 15 h. At preset time points, the surfaces were thoroughly rinsed with PBS. Next, all samples were stained with 1% (wt/vol) crystal violet solution for 15 min, then washed three times with PBS. Finally, 1 ml of 95% (v/v) ethanol was added to each well. The mixture was then incubated for 15 min in the dark and shocked for 10 s

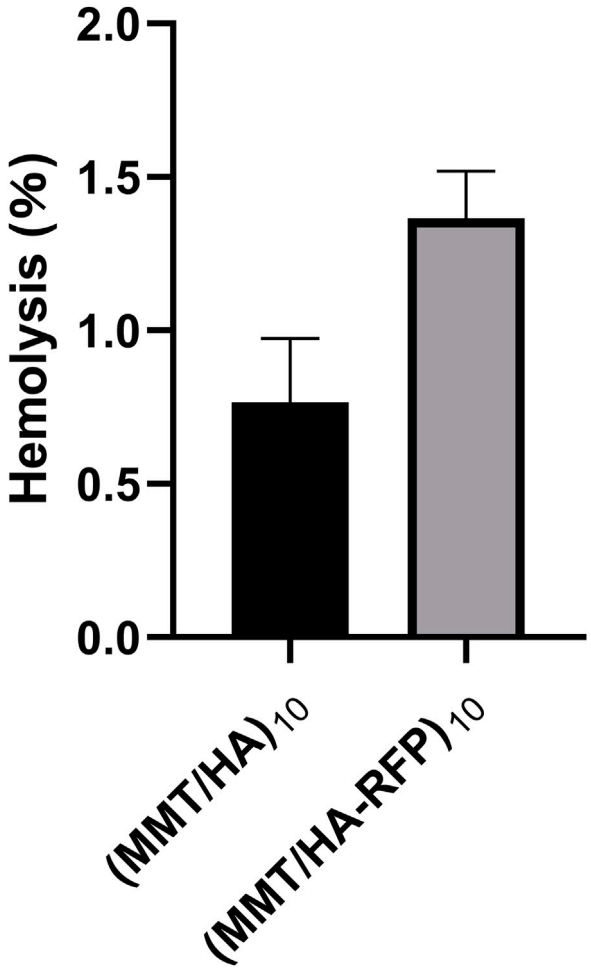

FIGURE 5
Hemolysis rates of $(MMT/HA)_{10}$ and $(MMT/HA\text{-}RFP)_{10}$ multilamellar films.

every 5 min at room temperature. The absorbance at 570 nm (A570) was measured with a microplate reader (BioTek, Winooski, VT, United States).

2.6 Shaking flask culture and live/dead staining assay

The shaking flask culture method was used to comprehensively evaluate the *in vitro* antibacterial properties of the coating. $(MMT/HA\text{-}RFP)_{10}$-coated polydimethylsiloxane was immersed in *S. aureus* solution and cultured. Aliquots of the bacterial solution were collected at specified time points (2 h, 4 h, 6 h, 8 h, 10 h, and 12 h) and diluted; next, they were evenly spread on agar plates, cultured, and counted. For direct analysis of the live/dead populations of bacteria on the surface of $(MMT/HA\text{-}RFP)_{10}$ multilamellar membrane structures, fluorescence microscopy was conducted with live/dead staining. $(MMT/HA\text{-}RFP)_{10}$-coated glass slides and unmodified glass slides were co-cultured with 3 ml of *S. aureus* solution, incubated at 37°C for 6, 12, or 24 h, and then subjected to live/dead staining.

2.7 *In vitro* hemolysis rate

Four ml of fresh anticoagulated rat blood was diluted with 5 ml of normal saline. The multilamellar film was incubated in 10 ml of normal saline (37°C constant temperature water bath, 30 min). Next, 0.2 ml of diluted blood was added by mixing, and the solution was incubated at a constant temperature of 37°C for 60 min. Aliquots of 500 μL were collected and centrifuged at 1,500 rpm for 5 min. The absorbance of the resulting supernatant at 540 nm was measured with an ultraviolet-visible spectrophotometer (PuXi TU-1800; China). In the positive control group, 0.2 ml of diluted blood was added to 10 ml of distilled water; in the negative control group, 0.2 ml of diluted blood was added to 10 ml of 0.9% NaCl solution.

Hemolysis of the multilamellar film was calculated using the following equation:

$$\text{Hemolysis rate \%} = (ODs - ODn)/(ODp - ODn) \times 100$$

where ODs, ODp, and ODn represent the respective absorbance values of the sample, negative control, and positive control groups.

2.8 Animal experiments

2.8.1 Biocompatibility analysis

Thirty male rats (body weight 200 ± 20 g) were obtained from SLAC Laboratory Animal Co., Ltd. (Shanghai, China) for use in this experiment. All experiments were approved by the Animal Research Ethics Committee of the Second Affiliated Hospital (Jiande Branch) of the School of Medicine, Zhejiang University. All rats were housed in an animal room with controlled humidity and temperature, where they were provided with adequate food and water. Unmodified, $(MMT/HA)_{10}$-coated, and $(MMT/HA\text{-}RFP)_{10}$ multilamellar film-coated K-wires were prepared. The rats were randomly divided into three groups (n = 10 per group). For the experimental analysis, the rats were initially anesthetized with 10% chloral hydrate (0.35 ml/100 g). The left knee of each rat was shaved, the overlying fur was removed, and the skin was disinfected. Then, the skin and muscles were cut to expose the tibial plateau. During this procedure, neurovascular injury was avoided when possible. Under sterile conditions, a 0.8-mm K-bit was used to drill vertically into the medullary cavity, and a sterile syringe was used to aspirate bone marrow from the tibia. Unmodified, $(MMT/HA)_{10}$-coated, or $(MMT/HA\text{-}RFP)_{10}$ multilamellar film-coated K-wires were placed in the boreholes according to each rat's group designation. The drilled hole was sealed with bone wax, and the incision was sutured layer by layer. After each rat had regained consciousness, it was

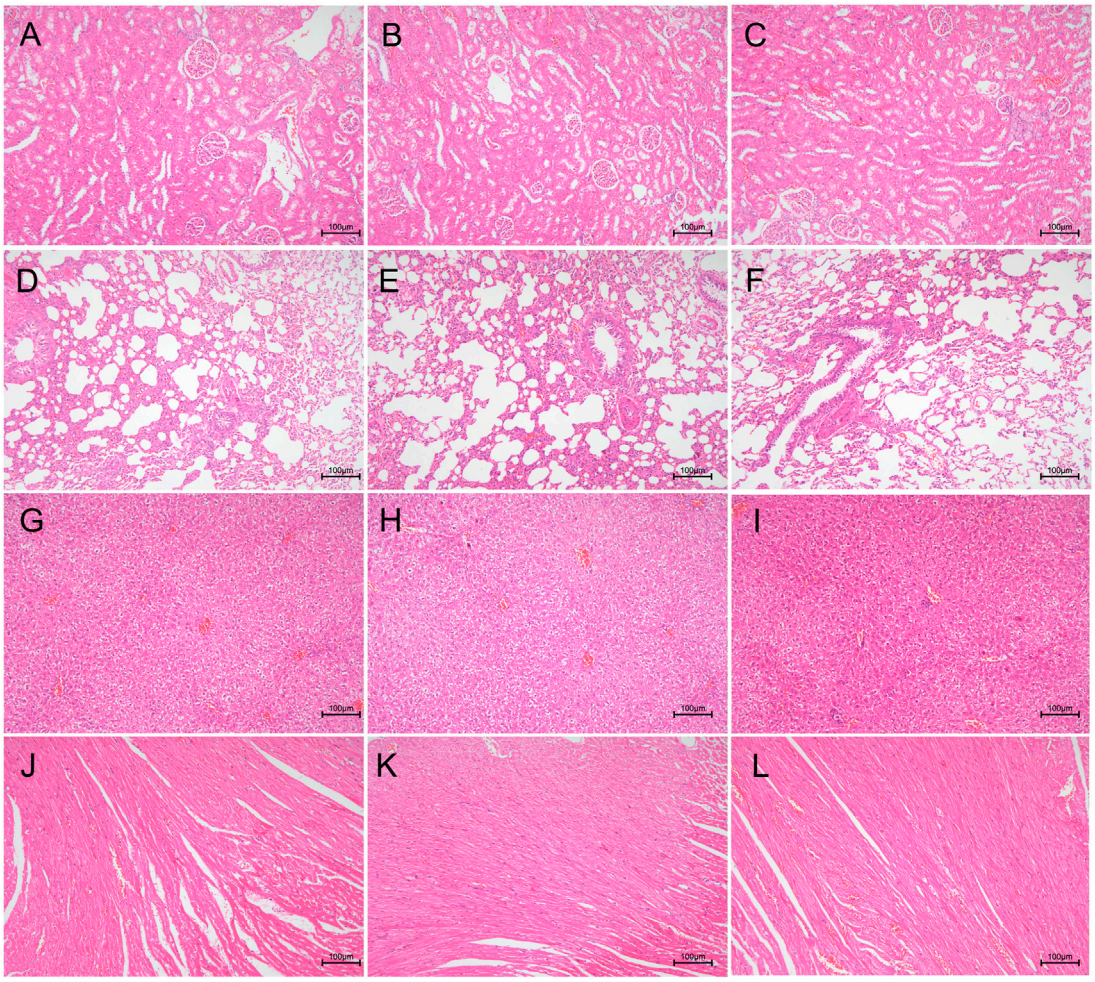

FIGURE 6
Biocompatibility analysis of $(MMT/HA)_{10}$ and $(MMT/HA\text{-}RFP)_{10}$ multilamellar films. H&E staining of rat kidney, lung, liver, and heart. **(A–C)** Kidney in the unmodified, $(MMT/HA)_{10}$, and $(MMT/HA\text{-}RFP)_{10}$ groups, respectively. **(D–F)** Lung in the unmodified, $(MMT/HA)_{10}$, and $(MMT/HA\text{-}RFP)_{10}$ groups, respectively. **(G–I)** Liver in the unmodified, $(MMT/HA)_{10}$, and $(MMT/HA\text{-}RFP)_{10}$ groups, respectively. **(J–L)** Heart in the unmodified, $(MMT/HA)_{10}$, and $(MMT/HA\text{-}RFP)_{10}$ groups, respectively.

maintained in an appropriate environment with adequate food and water. All rats were sacrificed 4 weeks after surgery. Their tissues (lung, kidney, heart, and liver) were cryopreserved, cut into sections, fixed, and stained with hematoxylin and eosin (H&E), in accordance with standard protocols.

2.8.2 *In vivo* antibacterial experiments

Thirty additional rats were used to determine the *in vivo* antimicrobial efficacy of the multilamellar film structure. The animals were divided randomly into three groups (n = 10 per group): 1) an unmodified group, with placement of unmodified K-wires and injection of 10 μL of 10^6 *S. aureus* cells/mL; 2) a $(MMT/HA\text{-}RFP)_{10}$ group, with placement of $(MMT/HA\text{-}RFP)_{10}$-coated K-wires and injection of 10 μL of 10^6 *S. aureus* cells/mL; and 3) a sham group, with placement of unmodified K-wires and without injection of *S. aureus*. For each animal, the drilled hole was sealed with bone wax, and the incision was sutured layer by layer. After each rat had regained consciousness, it was maintained in a standard environment with adequate food and water. The condition of each wound was monitored regularly.

2.8.2.1 Measurement of body temperature and inflammatory index *in vivo*

At regular intervals, each rat's body temperature was monitored and their blood collected from the tail tip to examine white blood cell (WBC) count, as well as levels of high-sensitivity C-reactive protein (hs-CRP), interleukin (IL)-1β, IL-6, and IL-8.

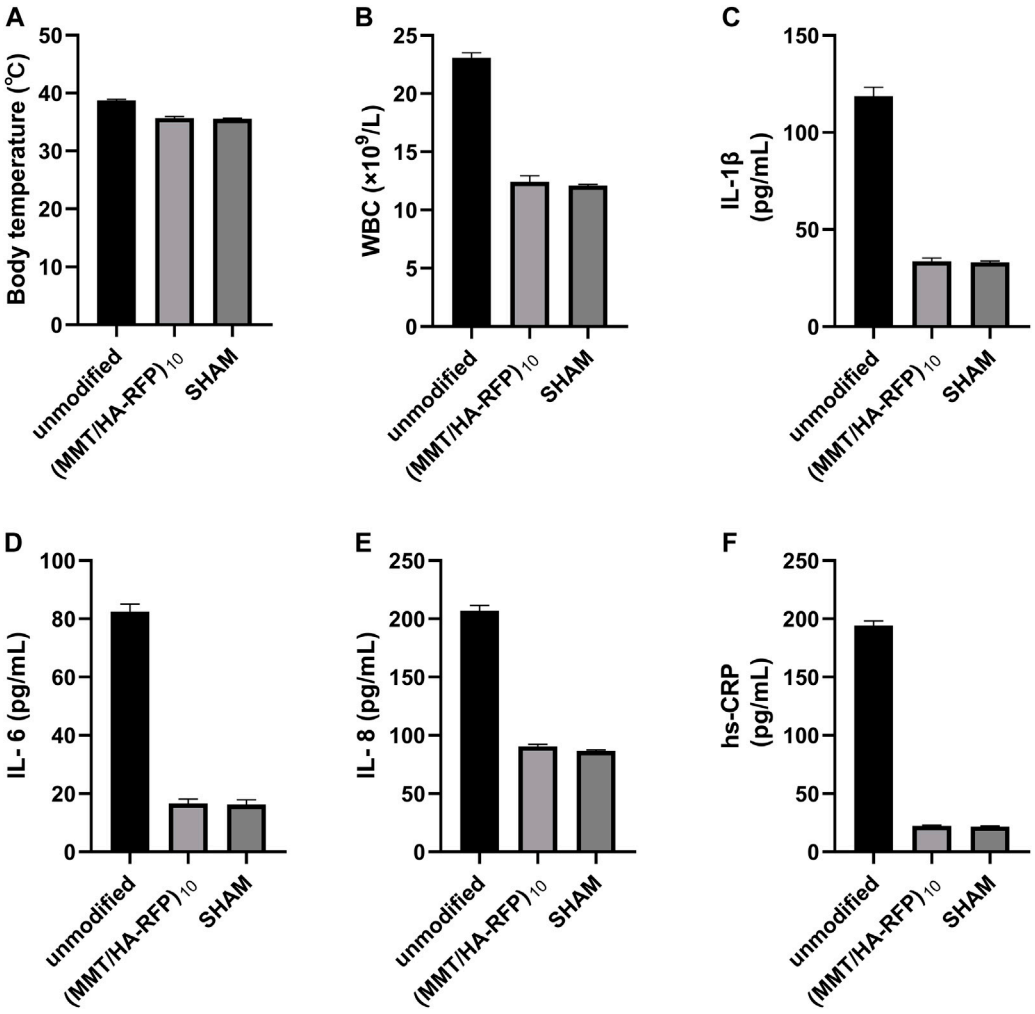

FIGURE 7
(A) Body temperature, **(B)** WBC count, **(C)** IL-1β level, **(D)** IL-6 level, **(E)** IL-8 level, and **(F)** hs-CRP level in rats.

2.8.2.2 Colonies from K-wires and soft tissue

Left tibia specimens were thawed at room temperature, then snap-frozen in liquid nitrogen. The soft tissue was pulverized in sterile PBS for 60 s. Concurrently, the K-wires were sonicated in sterile PBS for 30 min. All procedures were performed in a sterile environment. The fluids from soft tissue and K-wires were diluted in sterile saline, inoculated onto agar plates, and placed in a bacteriological incubator at a constant temperature of 37°C. Finally, the numbers of bacterial colonies on agar plates were counted.

2.8.2.3 X-ray examination

Each rat was euthanized and their left tibia extracted for X-ray examination (current, 250 mA; energy, 45 kV; integration time, 200 ms) (Carestream DRX; Carestream, Rochester, NY, United States). Three deputy chief orthopedic physicians evaluated the tibia destruction, osteolytic lesions, and tissue surrounding the tibia. Then, each tibia was wrapped in saline-saturated gauze and stored at −20°C.

2.8.2.4 Computed tomography examination

Left tibia specimens were thawed at room temperature and their soft tissue removed. Next, the samples were fixed with 4% paraformaldehyde in PBS for 12 h. Tibia lesions were observed by CT (energy, 70 kV at 114 μA; integration time, 300 ms; threshold, 220) (Skyscan 1,173; Skyscan, Kontich, Belgium). A ring with a surface radius of 0.1 mm from the metal implant was evaluated as the volume of interest. CT software was used to analyze bone mineral density (BMD), trabecular bone number (Tb.N),

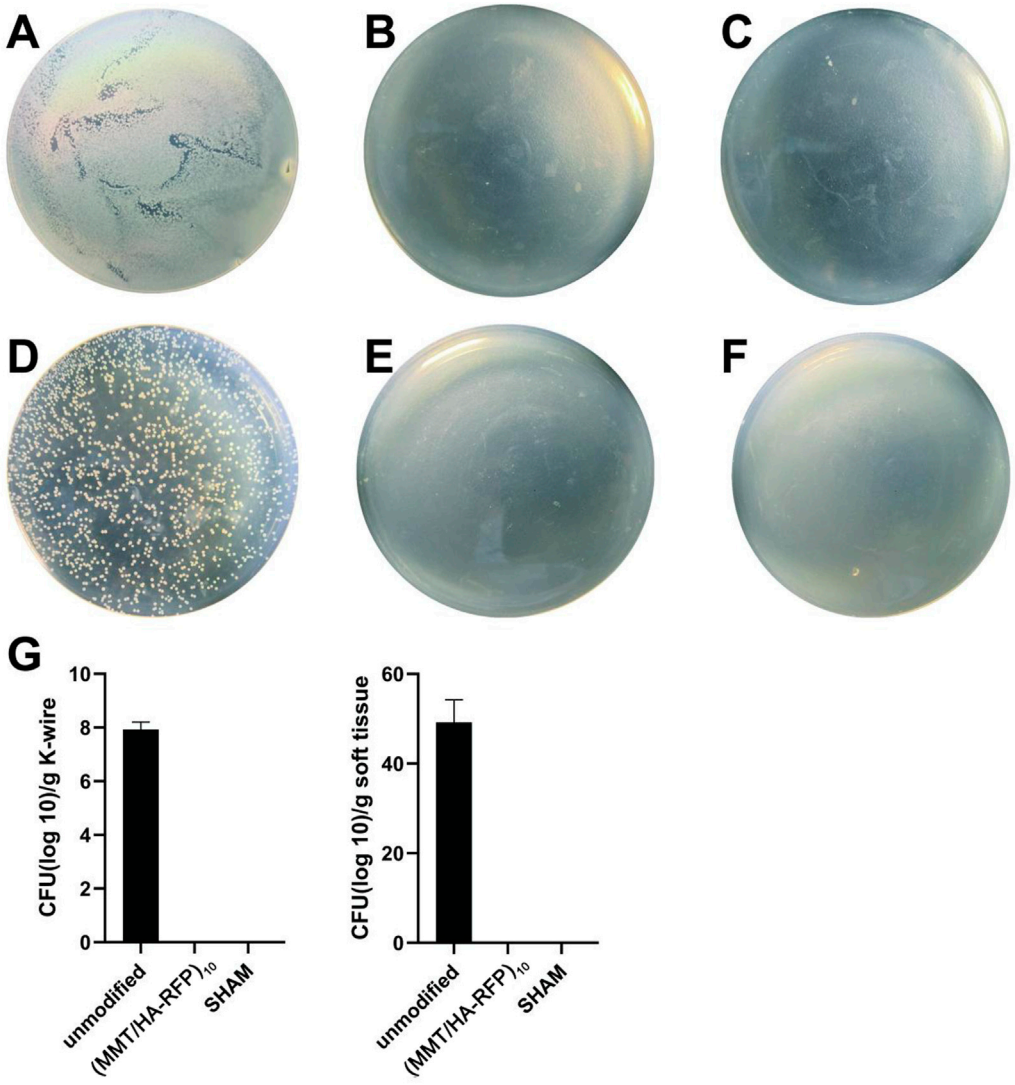

FIGURE 8
Colonies from K-wires: **(A–C)** unmodified, $(MMT/HA\text{-}RFP)_{10}$, and sham groups, respectively. Colonies from soft tissue: **(D–F)** unmodified, $(MMT/HA\text{-}RFP)_{10}$, and sham groups, respectively. **(G)** Number of colonies in each group.

percentage bone volume (BV/TV), and trabecular thickness (Tb.Th); three-dimensional histograms were also constructed.

2.8.2.5 Tibia specimen bending test

Left tibia specimens were thawed at room temperature and their soft tissue removed. The specimens were subjected to three-point bending tests to determine their integration strength, using an ElectroForce 3200 computer-controlled testing machine (Bose Corp., Eden Prairie, MN, United States); a crosshead speed of 1 mm min−1 was applied until each specimen broke. Finally, the maximum load, maximum strain, maximum bending moment, maximum stress, and bending section modulus were determined for the quantitative analysis of the mechanical strength of each tibia.

2.8.2.6 Histological analysis

Lesions of the tibial metaphysis were fixed with 4% paraformaldehyde for 48 h. Tibia bone specimens were decalcified with ethylenediaminetetraacetic acid solution for

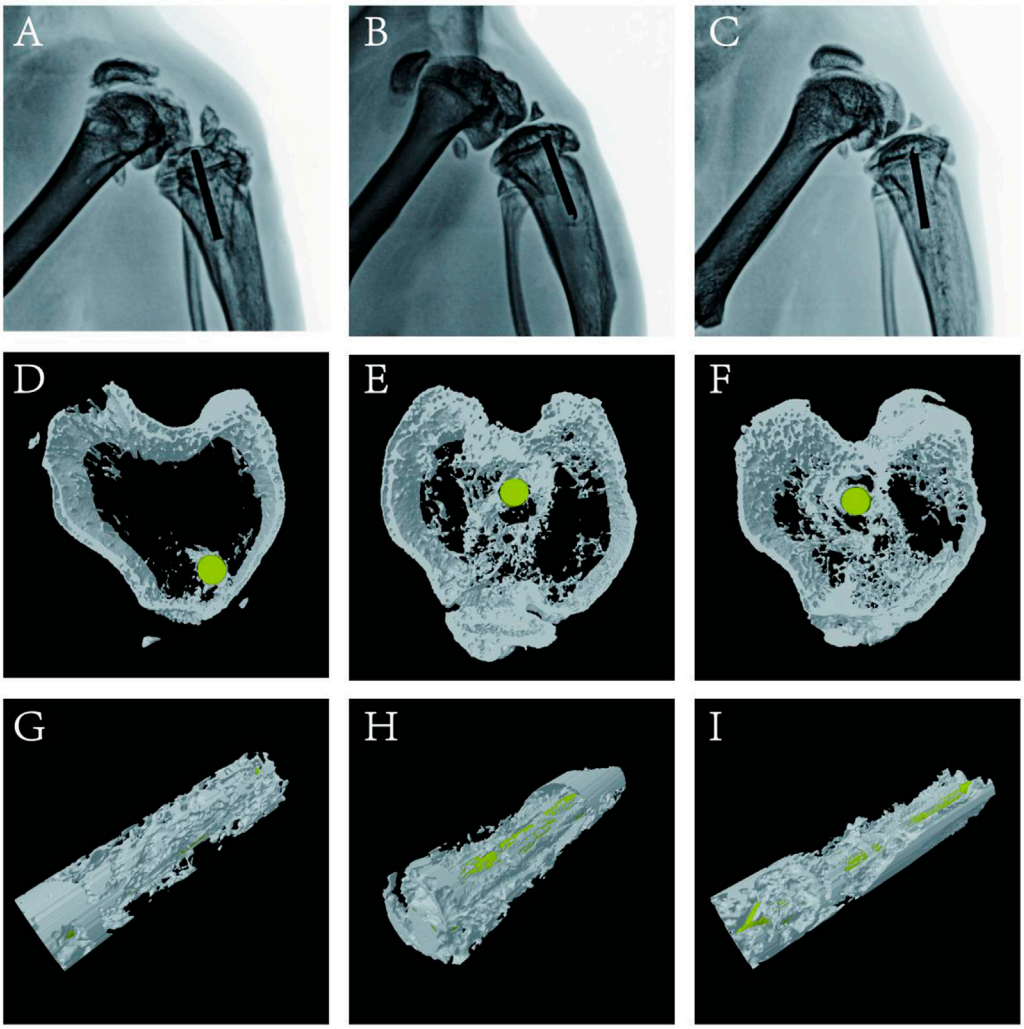

FIGURE 9
X-ray examination: **(A–C)** unmodified, $(MMT/HA\text{-}RFP)_{10}$, and sham groups, respectively. Trabecular distribution: **(D–F)** unmodified, $(MMT/HA\text{-}RFP)_{10}$, and sham groups, respectively. New bone formation surrounding implants: **(G–I)** unmodified, $(MMT/HA\text{-}RFP)_{10}$, and sham groups, respectively.

one month, then embedded in paraffin. The specimens were cut into 5-μm-thick sections; stained with H&E, Masson's trichrome, and toluidine blue; and then observed under a microscope.

2.9 Statistical analysis

Data analyses were performed using SPSS 24.0 (SPSS Inc., Chicago, IL, United States). Multisample means were evaluated by one-way analysis of variance ($\alpha = 0.05$). Comparisons among groups were analyzed by the *t*-test. In all analyses, $p < 0.05$ was considered to indicate statistical significance.

3 Results and discussion

3.1 Characterization of materials

As shown in Figure 1, we measured the roughness of surfaces using atomic force microscopy (AFM). After the coating was deposited, surface roughness increased. More specifically, the $(MMT/HA\text{-}RFP)_{0.5}$ coating had a roughness of 8.70 ± 4.14 nm, and the $(MMT/HA\text{-}RFP)_3$ coating had a roughness of 285.33 ± 12.71 nm. The roughness of the $(MMT/HA\text{-}RFP)_7$ coating was 489.33 ± 9.03 nm, that of the $(MMT/HA\text{-}RFP)_{10}$ coating was 630.00 ± 21.74 nm, and that of the $(MMT/HA)_{10}$ coating was

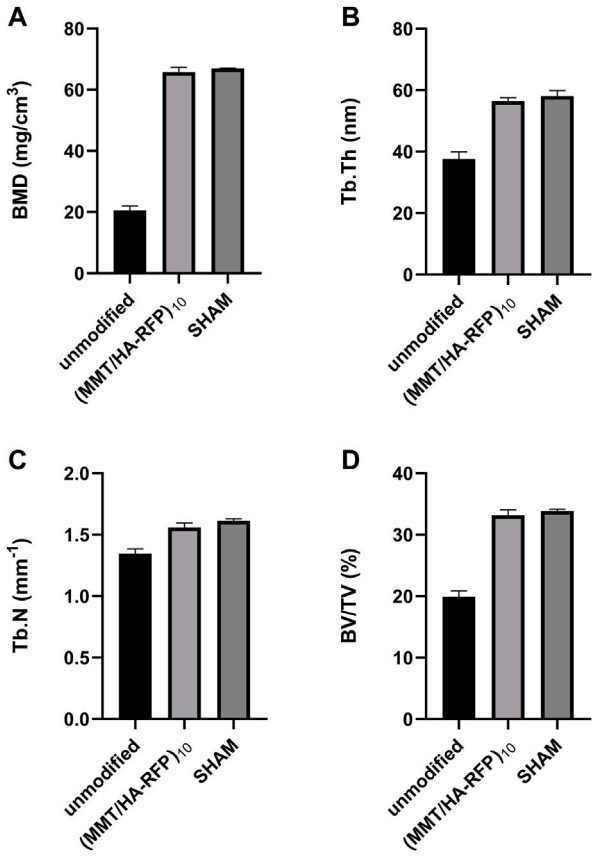

FIGURE 10
Analysis of **(A)** BMD, **(B)** Tb.Th, **(C)** Tb.N, and **(D)** BV/TV in each group.

599.67 ± 22.07 nm. Using SEM, we observed multiple layers on the surface of substrate, with uniform membrane structure. Next, the contact angle was measured to determine the hydrophilicity of each surface. The contact angles were 26.30 ± 1.10° for the $(MMT/HA\text{-}RFP)_{0.5}$ coating, 40.20 ± 1.56° for the $(MMT/HA\text{-}RFP)_3$ coating, 45.37 ± 0.63° for the $(MMT/HA\text{-}RFP)_7$ coating, and 47.43 ± 0.63° for the $(MMT/HA\text{-}RFP)_{10}$ coating. In addition, the contact angle of the $(MMT/HA)_{10}$ coating was 46.13 ± 0.42°. This shows that the material has a hydrophilic surface after coating modification. Many reports have indicated that moderate hydrophilicity could increase the biocompatibility of the material (Bluestein et al., 2017; Hu et al., 2017). Finally, we performed thickness measurements on multilayer structures. The thickness of the multilamellar membrane structures clearly exhibited linear growth as assembly progressed. More specifically, the thickness of the $(MMT/HA\text{-}RFP)_1$ coating was 23.33 ± 5.79 nm. As self-assembly progressed, the $(MMT/HA\text{-}RFP)_5$ coating had a thickness of 319.67 ± 9.46 nm and the $(MMT/HA\text{-}RFP)_{10}$ coating had a thickness of 557.00 ± 5.10 nm.

3.2 ZOI measurement and SEM

The ZOI represents the diameter of the bacteriostatic area, which reflects the antibacterial coating of the multilamellar films. As shown in Figure 2, after immersion in 0.01 M PBS, the ZOI around the multilamellar films was 2.93 ± 0.14 cm, whereas it was 4.59 ± 0.14 cm and 5.43 ± 0.06 cm after immersion in HAS solutions at concentrations of 90 and 120 U/mL, respectively. After multilamellar films had been immersed in solutions containing 105 or 106 colony-forming units/mL of *S. aureus*, the ZOIs were 4.86 ± 0.05 cm and 5.87 ± 0.20 cm, respectively. Changes in the multilamellar coating on the surfaces of glass slides were examined by SEM. Compared with immersion in PBS, the degree of disintegration of the $(MMT/HA\text{-}RFP)_{10}$ multilamellar film structure gradually increased after two days of immersion in solutions with increasing concentrations of HAS and *S. aureus*. The ZOI increase with increasing concentrations of HAS and bacterial solutions may have occurred because the HAS secreted by *S. aureus* promoted the disintegration of the multilamellar film,

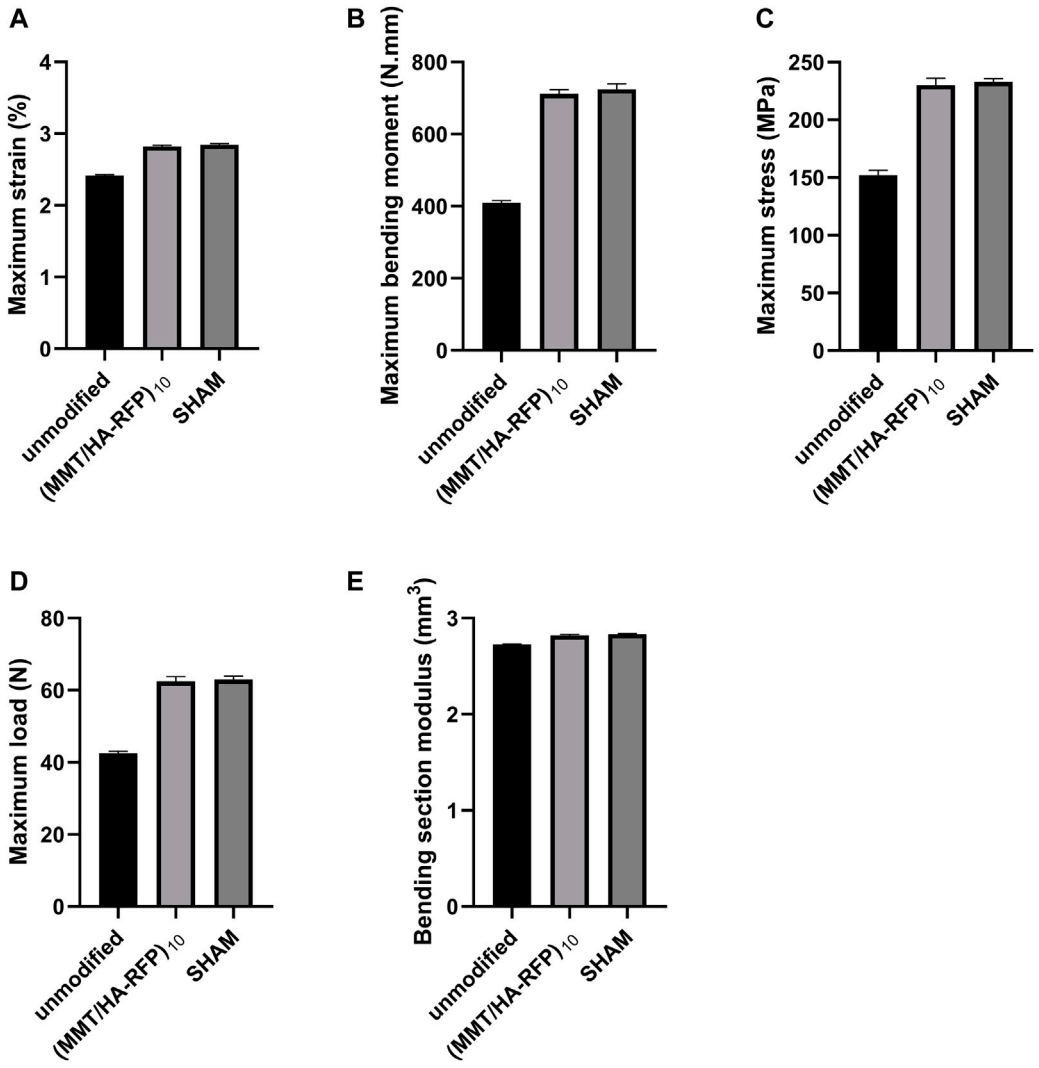

FIGURE 11
Bending tests of tibia specimens: **(A)** maximum strain, **(B)** maximum bending moment, **(C)** maximum stress, **(D)** maximum load, **(E)** bending section modulus.

leading to large amounts of disintegrated film fragments on the surface of the glass slides, and MMT could be loaded with large amounts of the test drug.

3.3 Determination of biofilm formation

Biofilm inhibition activity was assessed by crystal violet staining (Figure 3). The crystal violet absorption by the $(MMT/HA\text{-}RFP)_{10}$ samples was substantially lower than the crystal violet absorption by the unmodified samples at all time points examined (5, 10, and 15 h). With increasing culture time, the crystal violet absorption by all $(MMT/HA\text{-}RFP)_{10}$ samples slowly increased, whereas the crystal violet absorption by unmodified samples substantially increased, confirming that the $(MMT/HA\text{-}RFP)_{10}$ multilamellar film structure had strong biofilm-inhibition effects.

3.4 Shaking flask culture and live/dead staining assay

The number of bacteria was calculated at various time points using the shaking flask method. As shown in Figure 4, the number of bacteria decreased over time, nearly reaching zero at 12 h, indicating that the antibacterial coating can

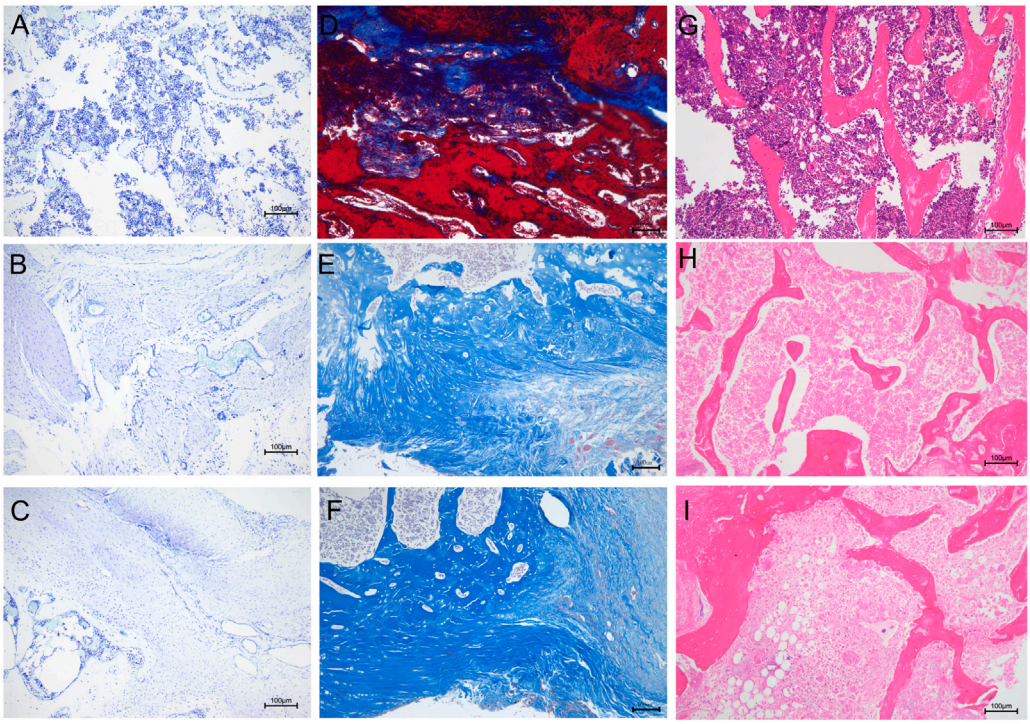

FIGURE 12
Histological analysis. Toluidine blue staining: **(A–C)** unmodified, $(MMT/HA\text{-}RFP)_{10}$, and sham groups, respectively. Masson's trichrome staining: **(D–F)** unmodified, $(MMT/HA\text{-}RFP)_{10}$, and sham groups, respectively. H&E staining: **(G–I)** unmodified, $(MMT/HA\text{-}RFP)_{10}$, and sham groups, respectively.

rapidly and efficiently sterilize bacterial solutions. After 6, 12, and 24 h of coincubation, the numbers of both live (green) and dead (red) bacteria were substantially reduced on the surface of the $(MMT/HA\text{-}RFP)_{10}$ multilamellar film, compared with the unmodified group. These observations indicate that the $(MMT/HA\text{-}RFP)_{10}$ polymer multilamellar film has excellent antibacterial properties. The $(MMT/HA\text{-}RFP)_{10}$ multilamellar membrane structure may also remove some dead bacteria from the surface.

3.5 *In vitro* hemolysis rate

The hemolysis rate represents the degree of damage to red blood cells caused by the test material, which is an important consideration in the experimental analysis of medical materials (Figure 5). The absorbance value of the positive control group (ODp) was 1.225 L/g/cm, whereas the absorbance value of the negative control group (ODn) was 0.001 L/g/cm. The absorbance values of the sample (ODs) were substituted into the formula specified in the Methods to calculate the hemolysis rate. The hemolysis rate of the membrane surface was <5%, consistent with the standard for medical polymer materials, and the multilayer structure fulfilled the requirements of the body environment (Dang et al., 2019).

3.6 Biosafety evaluation

To evaluate the biocompatibility of the $(MMT/HA\text{-}RFP)_{10}$ multilamellar membrane structure, H&E-stained vital organ sections were subjected to histological examination. Heart, liver, lung, and kidney sections from the $(MMT/HA)_{10}$ and $(MMT/HA\text{-}RFP)_{10}$ groups exhibited normal morphology (Figure 6). Therefore, the $(MMT/HA\text{-}RFP)_{10}$ multilamellar membrane structure demonstrated excellent biocompatibility.

3.7 Measurement of body temperature and inflammatory index *in vivo*

A rat infection model was used to explore the *in vivo* antibacterial properties of $(MMT/HA\text{-}RFP)_{10}$ multilamellar films. Body temperature and WBC count, as well as levels of hs-CRP, IL-1β, IL-6, and IL-8, were examined to characterize

infection control. At 4 weeks after surgery, body temperature in the sham group was normal (35.57°C ± 0.09°C), whereas body temperature in the unmodified group had significantly increased to 38.73°C ± 0.17°C. However, body temperature in the $(MMT/HA\text{-}RFP)_{10}$ group was 35.67°C ± 0.25°C (Figure 7A), presumably because the $(MMT/HA\text{-}RFP)_{10}$ multilamellar film released antibiotics that killed bacteria; no rats in that group exhibited postoperative infection. Moreover, WBC count in the unmodified group was elevated at 4 weeks after surgery but within normal limits in the $(MMT/HA\text{-}RFP)_{10}$ group (Figure 7B). Similar trends were observed in the levels of IL-1β (Figure 7C), IL-6 (Figure 7D), IL-8 (Figure 7E) and hs-CRP (Figure 7F).

3.8 Colonies isolated from K-wires and soft tissue

Bacteriological examination revealed large amounts of bacteria on K-wires and in soft tissue in the unmodified group (Figures 8A,D), indicating that bacteria spread *via* circulation and multiplied throughout the body. However, there were no bacteria in the $(MMT/HA\text{-}RFP)_{10}$ group (Figures 8B,E). As expected, there were also no bacteria in the sham group (Figures 8C,F). Compared with the unmodified group, the surfaces of the K-wires and soft tissue in the $(MMT/HA\text{-}RFP)_{10}$ group showed 7.93 ± 0.23 and 49.20 ± 4.12 log reductions of *S. aureus*, respectively (Figure 8G).

3.9 X-ray and CT examination

Bone infection is commonly assessed by X-ray examination in clinical practice (Mistry et al., 2016). Bone in the sham group exhibited excellent structural integrity (Figure 9C), confirming that the surgeries had been performed successfully, animal management was reliable, and no infections had occurred. The unmodified group exhibited bone destruction on the tibial plateau, and the femoral condyle was infected (Figure 9A). These phenomena may have occurred because bacteria multiplied throughout the body and severely damaged the bone structure. Notably, no bone destruction was observed in the $(MMT/HA\text{-}RFP)_{10}$ group, despite injection of *S. aureus* into the bone (Figure 9B). To comprehensively assess bone tissue microstructure, three-dimensional histograms were constructed using the software provided with the CT scanner. K-wires appeared yellow on cross-sections of rat tibia. Trabecular bone constitutes the internal extension of cortical bone in the bone marrow cavity. There is an irregular network structure inside, which supports hematopoietic function; this microstructure is extremely difficult to segment within the bone (Kesavan et al., 2017). As shown in Figure 9D, the unmodified group exhibited the widespread rupture and disordered arrangement of trabecular bone. However, the $(MMT/HA\text{-}RFP)_{10}$ and sham groups exhibited considerably less trabecular bone destruction (Figures 9E,F). Moreover, minimal new bone formation was visible in the unmodified group (Figure 9G). In contrast, a considerable amount of new bone was detected around implants in the $(MMT/HA\text{-}RFP)_{10}$ group; the new bone was in close contact with the implant surface (Figure 9H). Importantly, the findings were similar between the $(MMT/HA\text{-}RFP)_{10}$ and sham groups (Figure 9I). Furthermore, micro-CT was performed to quantify BMD, Tb.N, BV/TV, and Tb.Th (Figure 10). In the sham group, the tibia lesions demonstrated normal values of BMD, Tb.N, BV/TV, and Tb.Th. In the unmodified group, the presence of bacteria led to significant decreases in the tibial total BMD, Tb.N, BV/TV, and Tb.Th. Bacterial proliferation affects bone cell growth (Min et al., 2016). Surprisingly, all characteristics in the $(MMT/HA\text{-}RFP)_{10}$ group resembled characteristics in the sham group.

3.10 Bending tests of tibia specimens

The three-point bending test was used to examine the integration strength of bone samples in each group through assessments of maximum load, maximum strain, maximum bending moment, maximum stress, and bending section modulus. As shown in Figure 11, tibia lesions in the sham group had normal values for maximum load, maximum strain, maximum bending moment, maximum stress, and bending section modulus. However, all values were significantly lower in the unmodified group. Bacteria can reportedly disrupt homeostatic balance in bone and destroy the integrity of bone microstructure (Raphel et al., 2016). Importantly, all characteristics in the $(MMT/HA\text{-}RFP)_{10}$ group resembled characteristics in the sham group, confirming that the $(MMT/HA\text{-}RFP)_{10}$ multilamellar membrane structure has good antibacterial properties.

3.11 Histological analysis

We performed further histological analyses by staining bone sections with H&E, Masson's trichrome, and toluidine blue. Toluidine blue staining showed numerous mast cells in the bone tissue of the unmodified group (Figure 12A). Mast cells can release large amounts of inflammatory mediators, such as tumor necrosis factor-α, IL-1, and IL-8 (Delgado et al., 2020). However, inflammatory mast cell infiltration was significantly

reduced in the $(MMT/HA\text{-}RFP)_{10}$ group (Figure 12B). In the sham group, mast cells were not observed, and the bone tissue structure was normal (Figure 12C). Furthermore, the sections were subjected to Masson's trichrome staining to visualize collagen fibers and assess fibrotic lesions in bone tissue (Griffin et al., 2019). In the unmodified group, most areas were stained red because of infection-induced fibrosis in the bone marrow cavity (Figure 12D). Notably, bone tissue was completely free of fibrotic lesions in the $(MMT/HA\text{-}RFP)_{10}$ and sham groups (Figures 12E, 2F). H&E staining revealed that large quantities of inflammatory cells had penetrated the bone trabecula in the unmodified group, which confirmed the presence of bone infection (Figure 12G). However, no inflammatory responses (e.g., swelling or inflammatory cell infiltration) were found in the $(MMT/HA\text{-}RFP)_{10}$ and sham groups (Figures 12H,I).

4 Conclusion

In this study, a $(MMT/HA\text{-}RFP)_{10}$ multilamellar film structure was successfully prepared from MMT, HA, and RFP; its thickness increased linearly during layer-by-layer assembly. The $(MMT/HA\text{-}RFP)_{10}$ multilamellar film structure gradually deteriorated and exhibited concentration-dependent degradation during incubation with solutions containing HAS and *S. aureus*. The $(MMT/HA\text{-}RFP)_{10}$ multilamellar film structure showed good antibacterial properties, as determined by analyses of biofilm formation and shaking flask culture. The hemolysis rate highlighted the excellent biocompatibility of this material. $(MMT/HA\text{-}RFP)_{10}$ multilamellar film-coated K-wires showed excellent antibacterial properties and excellent biocompatibility *in vivo*. Further studies are needed to fully characterize the clinical potential of this material.

Data availability statement

The original contributions presented in the study are included in the article/Supplementary Material; further inquiries can be directed to the corresponding author.

Ethics statement

The animal study was reviewed and approved by the Animal Research Ethics Committee of the Second Affiliated Hospital (Jiande Branch) of the School of Medicine, Zhejiang University. Written informed consent was obtained from the owners for the participation of their animals in this study.

Author contributions

XB: conceptualization, methodology, software, investigation, formal analysis, writing—original draft; JY: data curation, writing—original draft; JX: visualization, investigation; YW: resources, supervision; ZL: software, validation; HW: conceptualization, funding acquisition, resources, supervision, writing—review and editing).

Acknowledgments

We thank all study participants.

Conflict of interest

The authors declare that the research was conducted in the absence of any commercial or financial relationships that could be construed as a potential conflict of interest.

Publisher's note

References

Amerstorfer, F., Fischerauer, S., Sadoghi, P., Schwantzer, G., Kuehn, K., Leithner, A., et al. (2017). Superficial vancomycin coating of bone cement in orthopedic revision surgery: A safe technique to enhance local antibiotic concentrations. *J. Arthroplasty* 32 (5), 1618–1624. doi:10.1016/j.arth.2016.11.042

Araújo, T., Rodrigues, P., Santos, M., de Oliveira, J., Rosa, L., Bagnato, V., et al. (2018). Reduced methicillin-resistant *Staphylococcus aureus* biofilm formation in bone cavities by photodynamic therapy. *Photodiagnosis Photodyn. Ther.* 21, 219–223. doi:10.1016/j.pdpdt.2017.12.011

Aycan, D., and Alemdar, N. J. C. p. (2018). Development of pH-responsive chitosan-based hydrogel modified with bone ash for controlled release of amoxicillin. *Carbohydr. Polym.* 184, 401–407. doi:10.1016/j.carbpol.2017.12.023

Barnett, S., Peters, D., Hamilton, W., Ziran, N., Gorab, R., and Matta, J. J. T. J. o. a. (2016). Is the anterior approach safe? Early complication rate associated with 5090 consecutive primary total hip arthroplasty procedures performed using the anterior approach. *J. Arthroplasty* 31 (10), 2291–2294. doi:10.1016/j.arth.2015.07.008

Berger, L., Eichler, J., Ryll, E., Fischerauer, S., Raschke, M., Kolbitsch, A., et al. (2016). Advanced interlocking systems to improve heavy-load-bearing characteristics of flexible intramedullary nailing. *Mater. Sci. Eng. C* 68, 358–365. doi:10.1016/j.msec.2016.05.122

Bluestein, B., Reed, J., and Canavan, H. J. A. s. s. (2017). Effect of substrate storage conditions on the stability of "Smart" films used for mammalian cell applications. *Appl. Surf. Sci.* 392, 950–959. doi:10.1016/j.apsusc.2016.07.004

Braem, A., De Cremer, K., Delattin, N., De Brucker, K., Neirinck, B., Vandamme, K., et al. (2015). Novel anti-infective implant substrates: Controlled release of antibiofilm compounds from mesoporous silica-containing macroporous titanium. *Colloids Surfaces B Biointerfaces* 126, 481–488. doi:10.1016/j.colsurfb.2014.12.054

Branch-Elliman, W., Ripollone, J., O'Brien, W., Itani, K., Schweizer, M., Perencevich, E., et al. (2017). Risk of surgical site infection, acute kidney injury, and *Clostridium difficile* infection following antibiotic prophylaxis with vancomycin plus a beta-lactam versus either drug alone: A national propensity-score-adjusted retrospective cohort study. *PLoS Med.* 14 (7), e1002340. doi:10.1371/journal.pmed.1002340

Caroom, C., Moore, D., Mudaliar, N., Winkler, C., Murphree, J., Ratheal, I., et al. (2018). Intrawound vancomycin powder reduces bacterial load in contaminated open fracture model. *J. Orthop. Trauma* 32 (10), 538–541. doi:10.1097/bot.0000000000001259

Chabbi, J., Jennah, O., Katir, N., Lahcini, M., Bousmina, M., and El Kadib, A. J. C. p. (2018). Aldehyde-functionalized chitosan-montmorillonite films as dynamically-assembled, switchable-chemical release bioplastics. *Carbohydr. Polym.* 183, 287–293. doi:10.1016/j.carbpol.2017.12.036

Chen, W., Luo, G., Qiu, W., Lei, Q., Liu, L., Wang, S., et al. (2017). Mesoporous silica-based versatile theranostic nanoplatform constructed by layer-by-layer assembly for excellent photodynamic/chemo therapy. *Biomaterials* 117, 54–65. doi:10.1016/j.biomaterials.2016.11.057

Dang, Q., Li, C., Jin, X., Zhao, Y., and Wang, X. J. C. p. (2019). Heparin as a molecular spacer immobilized on microspheres to improve blood compatibility in hemoperfusion. *Carbohydr. Polym.* 205, 89–97. doi:10.1016/j.carbpol.2018.08.067

Delgado, S., Dehmel, S., Twisterling, E., Wichmann, J., Jonigk, D., Warnecke, G., et al. (2020). Disruptive anti-IgE inhibitors prevent mast cell-dependent early airway response in viable atopic lung tissue. *J. Allergy Clin. Immunol.* 145 (2), 719–722.e1. e1. doi:10.1016/j.jaci.2019.11.002

Downes, K., Cowden, C., Laskin, B., Huang, Y., Gong, W., Bryan, M., et al. (2017). Association of acute kidney injury with concomitant vancomycin and piperacillin/tazobactam treatment among hospitalized children. *JAMA Pediatr.* 171 (12), e173219. doi:10.1001/jamapediatrics.2017.3219

Enteshari Najafabadi, M., and Bagheri, H. J. M. a. (2017). Wireless electrochemical preparation of gradient nanoclusters consisting of copper(II), stearic acid and montmorillonite on a copper wire for headspace in-tube microextraction of chlorobenzenes. *Microchim. Acta* 185 (1), 80. doi:10.1007/s00604-017-2549-9

Flamant, Q., Caravaca, C., Meille, S., Gremillard, L., Chevalier, J., Biotteau-Deheuvels, K., et al. (2016). Selective etching of injection molded zirconia-toughened alumina: Towards osseointegrated and antibacterial ceramic implants. *Acta Biomater.* 46, 308–322. doi:10.1016/j.actbio.2016.09.017

Friedrich, E., and Washburn, N. J. B. (2017). Transport patterns of anti-TNF-α in burn wounds: Therapeutic implications of hyaluronic acid conjugation. *Biomaterials* 114, 10–22. doi:10.1016/j.biomaterials.2016.11.003

Girmenia, C., and Iori, A. J. E. o. o. d. s. (2017). An update on the safety and interactions of antifungal drugs in stem cell transplant recipients. *Expert Opin. Drug Saf.* 16 (3), 329–339. doi:10.1080/14740338.2017.1273900

Griffin, M., Kalaskar, D., and Butler, P. J. J. o. n. (2019). Argon plasma modified nanocomposite polyurethane scaffolds provide an alternative strategy for cartilage tissue engineering. *J. Nanobiotechnology* 17 (1), 51. doi:10.1186/s12951-019-0477-z

Gundtoft, P., Pedersen, A., Schønheyder, H., Møller, J., and Overgaard, S. J. O. (2017). One-year incidence of prosthetic joint infection in total hip arthroplasty: A cohort study with linkage of the Danish hip arthroplasty register and Danish microbiology databases. *Osteoarthr. Cartil.* 25 (5), 685–693. doi:10.1016/j.joca.2016.12.010

Hirschfeld, J., Akinoglu, E., Wirtz, D., Hoerauf, A., Bekeredjian-Ding, I., Jepsen, S., et al. (2017). Long-term release of antibiotics by carbon nanotube-coated titanium alloy surfaces diminish biofilm formation by Staphylococcus epidermidis. *Nanomedicine Nanotechnol. Biol. Med.* 13 (4), 1587–1593. doi:10.1016/j.nano.2017.01.002

Hu, W., Lu, S., Ma, Y., Ren, P., Ma, X., Zhou, N., et al. (2017). Poly(dopamine)-inspired surface functionalization of polypropylene tissue mesh for prevention of intra-peritoneal adhesion formation. *J. Mat. Chem. B* 5 (3), 575–585. doi:10.1039/c6tb02667b

Huang, W., Chen, S., Chiang, W., Huang, C., Lo, C., Chern, C., et al. (2016). Tumor microenvironment-responsive nanoparticle delivery of chemotherapy for enhanced selective cellular uptake and transportation within tumor. *Biomacromolecules* 17 (12), 3883–3892. doi:10.1021/acs.biomac.6b00956

Hwang, D., Kim, H., Li, F., Park, J., Kim, D., Park, J., et al. (2017). *In vivo* visualization of endogenous miR-21 using hyaluronic acid-coated graphene oxide for targeted cancer therapy. *Biomaterials* 121, 144–154. doi:10.1016/j.biomaterials.2016.12.028

Jennings, J., Carpenter, D., Troxel, K., Beenken, K., Smeltzer, M., Courtney, H., et al. (2015). Novel antibiotic-loaded point-of-care implant coating inhibits biofilm. *Clin. Orthop. Relat. Res.* 473 (7), 2270–2282. doi:10.1007/s11999-014-4130-8

Jones, Z., Brooks, A., Ferrell, Z., Grainger, D., and Sinclair, K. J. J. o. b. m. r. P. B. (2016). A resorbable antibiotic eluting bone void filler for periprosthetic joint infection prevention. *J. Biomed. Mat. Res.* 104 (8), 1632–1642. doi:10.1002/jbm.b.33513

Kendall, M., and Gorgone, M. J. I. j. o. s. (2018). Surgical site infection following open reduction and internal fixation of a closed ankle fractures: A retrospective multicenter cohort study. *Int. J. Surg.* 49, 60–61. doi:10.1016/j.ijsu.2017.12.012

Kesavan, C., Bajwa, N., Watt, H., and Mohan, S. J. B. r. (2017). Experimental repetitive mild traumatic brain injury induces deficits in trabecular bone microarchitecture and strength in mice. *Bone Res.* 5, 17042. doi:10.1038/boneres.2017.42

Klein, S., Nurjadi, D., Eigenbrod, T., and Bode, K. J. I. j. o. a. a. (2016). Evaluation of antibiotic resistance to orally administrable antibiotics in staphylococcal bone and joint infections in one of the largest University hospitals in Germany: Is there a role for fusidic acid? *Int. J. Antimicrob. Agents* 47 (2), 155–157. doi:10.1016/j.ijantimicag.2015.12.002

Kyriakidis, I., Tragiannidis, A., Munchen, S., and Groll, A. J. E. o. o. d. s. (2017). Clinical hepatotoxicity associated with antifungal agents. *Expert Opin. Drug Saf.* 16 (2), 149–165. doi:10.1080/14740338.2017.1270264

Li, M., Liu, X., Xu, Z., Yeung, K., Wu, S. J. A. a. m., and interfaces (2016). Dopamine modified organic-inorganic hybrid coating for antimicrobial and osteogenesis. *ACS Appl. Mat. Interfaces* 8 (49), 33972–33981. doi:10.1021/acsami.6b09457

Li, Z., Shizhao, S., Chen, M., Fahlman, B., Liu, D, Bi, H. J. M. s., et al. (2017). *In vitro* and *in vivo* corrosion, mechanical properties and biocompatibility evaluation of MgF 2 -coated Mg-Zn-Zr alloy as cancellous screws. *Mater. Sci. Eng. C* 75, 1268–1280. doi:10.1016/j.msec.2017.02.168

Liu, Y., Chen, D., Zhang, A., Xiao, M., Li, Z., Luo, W., et al. (2021). Composite inclusion complexes containing hyaluronic acid/chitosan nanosystems for dual responsive enrofloxacin release. *Carbohydr. Polym.* 252, 117162. doi:10.1016/j.carbpol.2020.117162

Mable, C., Fielding, L., Derry, M., Mykhaylyk, O., Chambon, P., and Armes, S. J. C. s. (2018). Synthesis and pH-responsive dissociation of framboidal ABC triblock copolymer vesicles in aqueous solution. *Chem. Sci.* 9 (6), 1454–1463. doi:10.1039/c7sc04788f

Min, J., Choi, K., Dreaden, E., Padera, R., Braatz, R., Spector, M., et al. (2016). Designer dual therapy nanolayered implant coatings eradicate biofilms and accelerate bone tissue repair. *ACS Nano* 10 (4), 4441–4450. doi:10.1021/acsnano.6b00087

Mistry, S., Roy, S., Maitra, N., Kundu, B., Chanda, A., Datta, S., et al. (2016). A novel, multi-barrier, drug eluting calcium sulfate/biphasic calcium phosphate biodegradable composite bone cement for treatment of experimental MRSA osteomyelitis in rabbit model. *J. Control. Release* 239, 169–181. doi:10.1016/j.jconrel.2016.08.014

Neumann, M., Strohm, P., Reising, K., Zwingmann, J., Hammer, T., Suedkamp, N. J. S. j. o. t., et al. (2016). Complications after surgical management of distal lower leg fractures. *Scand. J. Trauma Resusc. Emerg. Med.* 24 (1), 146. doi:10.1186/s13049-016-0333-1

Perez-Jorge, C., Arenas, M., Conde, A., Hernández-Lopez, J., de Damborenea, J., Fisher, S., et al. (2017). Bacterial and fungal biofilm formation on anodized titanium alloys with fluorine. *J. Mat. Sci. Mat. Med.* 28 (1), 8. doi:10.1007/s10856-016-5811-5

Pickett, J., Thompson, J., Sadowska, A., Tkaczyk, C., Sellman, B., Minola, A., et al. (2018). Molecularly specific detection of bacterial lipoteichoic acid for diagnosis of prosthetic joint infection of the bone. *Bone Res.* 6, 13. doi:10.1038/s41413-018-0014-y

Qiao, Z., Zhao, S., Wang, J., Wang, S., Wang, Z., and Guiver, M. J. A. C. (2016). A highly permeable aligned montmorillonite mixed-matrix membrane for CO2 separation. *Angew. Chem. Int. Ed.* 55 (32), 9321–9325. doi:10.1002/anie.201603211

Raphel, J., Holodniy, M., Goodman, S., and Heilshorn, S. J. B. (2016). Multifunctional coatings to simultaneously promote osseointegration and prevent infection of orthopedic implants. *Biomaterials* 84, 301–314. doi:10.1016/j.biomaterials.2016.01.016

Seroussi, E., Blum, S., Krifucks, O., Lavon, Y., and Leitner, G. J. P. o. (2018). Application of pancreatic phospholipase A2 for treatment of bovine mastitis. *PLoS ONE* 13 (8), e0203132. doi:10.1371/journal.pone.0203132

Sugii, M., Ferreira, F., Müller, K., Lima, D., Groppo, F., Imasato, H., et al. (2017). Physical, chemical and antimicrobial evaluation of a composite material containing quaternary ammonium salt for braces cementation. *Mater. Sci. Eng. C* 73, 340–346. doi:10.1016/j.msec.2016.12.084

Sun, M., Li, Q., Yu, H., Cheng, J., Wu, N., Shi, W., et al. (2021). Cryo-self-assembled silk fibroin sponge as a biodegradable platform for enzyme-responsive delivery of exosomes. *Bioact. Mat.* 8, 505–514. doi:10.1016/j.bioactmat.2021.06.017

Tessier, J., Moore, B., Putty, B., Gandhi, R., and Duane, T. J. S. i. (2016). Prophylactic gentamicin is not associated with acute kidney injury in patients with open fractures. *Surg. Infect. (Larchmt).* 17 (6), 720–723. doi:10.1089/sur.2015.086

Wang, B., Liu, H., Sun, L., Jin, Y., Ding, X., Li, L., et al. (2018). Construction of high drug loading and enzymatic degradable multilayer films for self-defense drug release and long-term biofilm inhibition. *Biomacromolecules* 19 (1), 85–93. doi:10.1021/acs.biomac.7b01268

Wang, P., Sun, J., Lou, Z., Fan, F., Hu, K., Sun, Y., et al. (2016). Assembly-induced thermogenesis of gold nanoparticles in the presence of alternating magnetic field for controllable drug release of hydrogel. *Adv. Mat.* 28 (48), 10801–10808. doi:10.1002/adma.201603632

Wang, X., Wu, J., Li, P., Wang, L., Zhou, J., Zhang, G., et al. (2018). Microenvironment-Responsive magnetic nanocomposites based on silver nanoparticles/gentamicin for enhanced biofilm disruption by magnetic field. *ACS Appl. Mat. Interfaces* 10 (41), 34905–34915. doi:10.1021/acsami.8b10972